American Journal of Nanosciences
2026, Vol. 10, No. 2, pp. 52–63
https://doi.org/10.11648/j.ajn.20261002.12

Research Article

Structural, Morphological, Magnetic, and Electrical Properties of $ZrFe_{2-x}Bi_xO_5$ Nanoparticles (x = 0, 0.25, 0.50, 0.75 and 1.00) Synthesized via Sol-gel Auto-Combustion

Avadhut Manage[1], Balachandra G. Hegde[1,*], Shidaling Matteppanavar[2]

[1]Department of Physics, Rani Channamma University, Belagavi, India

[2]Department of Physics, KLE Society's Basavaprabhu Kore Arts Science and Commerce College, Chikodi, India

Abstract

$ZrFe_{2-x}Bi_xO_5$ (x = 0, 0.25, 0.50, 0.75, 1.00) nanoparticles were synthesized using Sol-gel auto-combustion method and their structural, morphological, magnetic, and frequency-dependent electrical properties were systematically characterized at room temperature. X-ray diffraction analysis confirms single phase monoclinic C2/c formation for every composition, the principal interplanar spacing increases linearly from 2.9503 Å to 3.0034 Å, crystallite size decreases from 32.1 to 16.7 nm, and dislocation density grows nearly four times as x advances to unity. Scanning electron microscopy reveals a progressive transition from large, irregularly agglomerated grains to a finer, more densely packed nanoparticulate microstructure. All M-H loops measured over ±10 kOe identify soft ferromagnetic, multi-domain behavior (S < 0.5 throughout); saturation magnetization plummets from 16.46 to 1.67 emu g^{-1} while the coercive field rises from 102.24 to 182.22 G. Impedance measurements (100 Hz - 10 MHz) show that bulk resistance increases ten times over the substitution range, Nyquist plots fit to a two element equivalent circuit of two CPE-resistor pairs in series, and the extracted grain and grain-boundary resistances rise monotonically with x, establishing that Bi^{3+} incorporation progressively depletes the Fe^{3+}/Fe^{2+} charge carrier pool. The dielectric constant follows Maxwell-Wagner-Sillars behavior and decreases with both frequency and Bi content, while AC conductivity spectra display a characteristic dual-peak pattern attributed to space-charge polarization at grain boundaries at low frequency and grain-interior Fe hopping at high frequency, both peaks diminishes with increasing Bi content. The correlated structure-property picture presented here establishes the Bi-substituted $ZrFe_2O_5$ system as a candidate for compositionally tunable soft-magnetic and dielectric applications.

Keywords

$ZrFe_{2-x}Bi_xO_5$, AB_2O_5, Sol-gel Auto-combustion, Soft Ferromagnetism, Non Debye Relaxation, Maxwell-Wagner Polarization, Complex AC Conductivity

1. Introduction

The interplay of structural, magnetic, and dielectric degrees of freedom in complex transition-metal oxides has become one of the most fertile areas of contemporary material science research, driven equally by fundamental curiosity and by the de-

*Correspondence: Balachandra G. Hegde (bghegde@rcub.ac.in)

Received: 1 June 2026; **Accepted:** 10 June 2026; **Published:** 26 June 2026

mand for multifunctional ceramics in next-generation spintronics, high-frequency communication, magnetic hyperthermia, and energy-storage technologies [1-4]. Within this broad landscape, compounds of the general formula AB_2O_5 attract growing attention because the structural versatility of their cation sublattice-accommodating diverse A and B occupants while retaining the characteristic 3: 5 cation-to-oxygen stoichiometry translates directly into a correspondingly rich portfolio of tunable properties [5-10]. Pseudobrookite $TiFe_2O_5$, karrooite $MgTi_2O_5$, and the orthorhombic multiferroic $TbMn_2O_5$ illustrate distinct manifestations of this structural flexibility [7-10].

Zirconium iron oxide in the 1: 2: 5 stoichiometry ($ZrFe_2O_5$) occupies a structurally distinctive niche within the AB_2O_5 family. Its monoclinic C2/c crystal structure seats Zr^{4+} in an eight-coordinated polyhedron alongside two inequivalent Fe^{3+} sites in distorted octahedral environments, a connectivity that sustains frustrated spin pathways and active Fe^{3+}/Fe^{2+} charge-transfer channels [11]. Prior investigations have established that $ZrFe_2O_5$ nanoparticles display significant photocatalytic and Fenton-type reactivities and soft ferromagnetic behavior whose intensity depends sensitively on the synthesis protocol and annealing history [12-15]. The related compound $ZrFe_2O_4$ has attracted parallel interest as a magnetic nano catalyst for organic synthesis and photodegradation applications [16, 17]. Systematic investigations of the AC impedance and dielectric response of pure and Ni-doped $ZrFe_2O_5$ were reported in our prior study [11], which revealed non-Debye relaxation and characteristic dual-peak AC conductivity spectra, and provided the structural and compositional baseline for the present work.

Chemical substitution at the B (iron) site is the most direct route to modify the magnetic exchange network and electrical transport properties of $ZrFe_2O_5$ while preserving the host crystal structure. In our earlier investigation [11], Ni^{2+} doping (up to x = 0.05) produced modest but measurable changes in lattice parameters, grain morphology, saturation magnetization, and dielectric relaxation dynamics, attributable to the moderate size mismatch ($\delta r/r \approx 7\%$) between Ni^{2+} (0.69 Å) and Fe^{3+} (0.645 Å). Extending the approach to Bi^{3+} substitution (r = 1.03 Å [18]) magnifies this mismatch to nearly 60% and introduces three additional physical effects absent in the Ni-doped system: (i) far greater lattice strain per dopant unit, enabling structural tuning over a wider single-phase composition range; (ii) a stereochemical active $6s^2$ lone pair that distorts local oxygen coordination and creates anisotropic dielectric response [19]; and (iii) a completely spin-inactive substituent that quantitatively dilutes the iron magnetic sublattice without contributing any compensating moment unlike Ni^{2+} (2 μ_B). These features make Bi^{3+} a uniquely informative probe of the structural property relationships in this system.

The sol-gel auto-combustion synthesis route exploited here combines the stoichiometric homogeneity of wet-chemical precursor mixing with the rapid exothermic ignition that produces finely divided, phase-pure powders at relatively low processing temperatures, circumventing the coarse microstructures and impurity phases typical of high-temperature solid-state reactions [20, 21]. No comprehensive study of Bi-substituted $ZrFe_2O_5$ spanning the full x = 0-1.00 range, and covering XRD, SEM, magnetic hysteresis, complex impedance, dielectric, and AC conductivity properties simultaneously, appears in the published literature. The present paper addresses this gap.

2. Synthesis and Experimental Techniques

Nanocrystalline $ZrFe_{2-x}Bi_xO_5$ (x = 0, 0.25, 0.50, 0.75, 1.00) were prepared by the sol-gel auto-combustion method using citric acid as the organic fuel [20, 21]. Analytical reagent grade ferric nitrate [$Fe(NO_3)_3 \cdot 9H_2O$], bismuth nitrate [$Bi(NO_3)_3 \cdot 5H_2O$], zirconyl nitrate [$ZrO(NO_3)_2 \cdot 3H_2O$], and citric acid ($C_6H_8O_7$) were dissolved in deionized water maintaining an oxidizer-to-fuel molar ratio of 1: 1. The solution was heated with continuous stirring at 80 °C until a viscous, amber gel formed; raising the temperature to 120 °C induced spontaneous ignition, producing a voluminous ashy precursor within seconds. The product was collected, ground in an agate mortar, and calcined and sintered at 500 °C for 5 h to eliminate organic residues and forming pure phase.

Room-temperature PXRD patterns were recorded on a diffractometer using Cu K_α radiation (λ = 1.5406 Å) over 2θ = 10-90°. Surface morphology and elemental composition were examined by scanning electron microscopy coupled with energy-dispersive X-ray spectroscopy. Magnetic hysteresis loops were recorded at 300 K on a home-built vibrating sample magnetometer (VSM) [22] over ±10 kOe. For electrical measurements, sintered powders were mixed with 6 wt% poly(vinyl alcohol) binder, uniaxially pressed into 8 mm-diameter pellets at 50 kg cm^{-2}, heated at 500 °C for 5 h, and contact-coated with silver paste cured at 100 °C for 30 min. Frequency-dependent impedance, dielectric, and AC conductivity data were acquired on a Wayne Kerr 6500B impedance analyzer at 300 K over 100 Hz to 10 MHz.

3. Results and Discussion

3.1. X-ray Diffraction Analysis

Every reflection in the parent compound indexes on a monoclinic unit cell, space group C2/c (No. 15), consistent with the polyhedral framework comprising Zr^{4+} in eight-coordination and two inequivalent Fe^{3+} sites in distorted octahedra [11, 23, 24]. No secondary-phase reflections attributable to ZrO_2, Fe_2O_3, or Bi_2O_3 were detected, confirming single-phase formation across the entire substitution range. The dominant reflection near 30 °(2θ) shifts monotonically to 29.72 °as x rises to 1.00, while the associated interplanar spacing expands from 2.9503 Å to 3.0034 Å, a linear variation that obeys Vegard's law [25, 26] with a coefficient of determination R^2 = 0.9994. The driving force is the ionic-size mismatch between Fe^{3+} (r

= 0.645 Å) and Bi^{3+} (r = 1.03 Å) in six-fold coordination [18], a nearly 60% discrepancy that dilates the surrounding oxygen polyhedra at each Bi site, in accordance with Bragg's law [27].

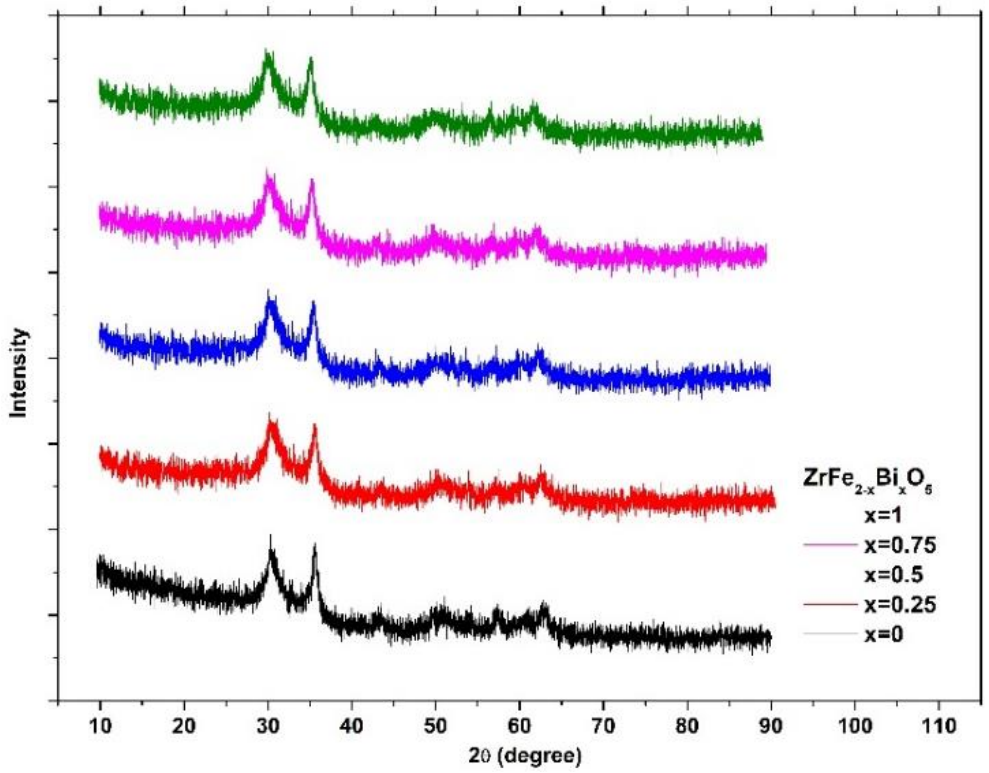

Figure 1. *Room temperature PXRD patterns of $ZrFe_2$−$xBixO_5$ compositions.*

Crystallite size D was evaluated from the Scherrer relation [28]. D contracts from 32.1 nm (x = 0) to 16.7 nm (x = 1.00), a 48% reduction, following the established trend of crystallite suppression under large-ion doping [29]. Williamson-Hall (W-H) plots [30] (β cosθ vs. 4 sinθ) provide the micro-strain ε from the gradient and confirm that all broadening trends are tensile: ε rises from 0.93 × 10^{-3} to 1.81 × 10^{-3}. Dislocation density ρ [31] climbs nearly four times from 3.08 to 11.34 × 10^{13} m^{-2}. No superlattice satellites appeared, confirming random Bi^{3+} distribution within the detection limit of the diffraction experiment. All derived parameters are given in Table 1.

Table 1. *XRD-derived structural and microstructural parameters for $ZrFe_{2-x}Bi_xO_5$ compositions.*

Composition (x)	2θ (°)	Interplanar Spacing d (Å)	Crystalline Size D (nm)	Micro-Strain (W-H) ε (10−3)	Dislocation Density $\rho = \frac{1}{D^2}$ (1013 m−2)
0	30.27	2.9503	32.1	0.93	3.08
0.25	30.13	2.9636	27.5	1.14	4.20
0.50	29.99	2.9768	23.8	1.36	5.59
0.75	29.86	2.9901	20.1	1.58	7.83
1.00	29.72	3.0034	16.7	1.81	11.34

3.2. Surface Morphology and EDAX

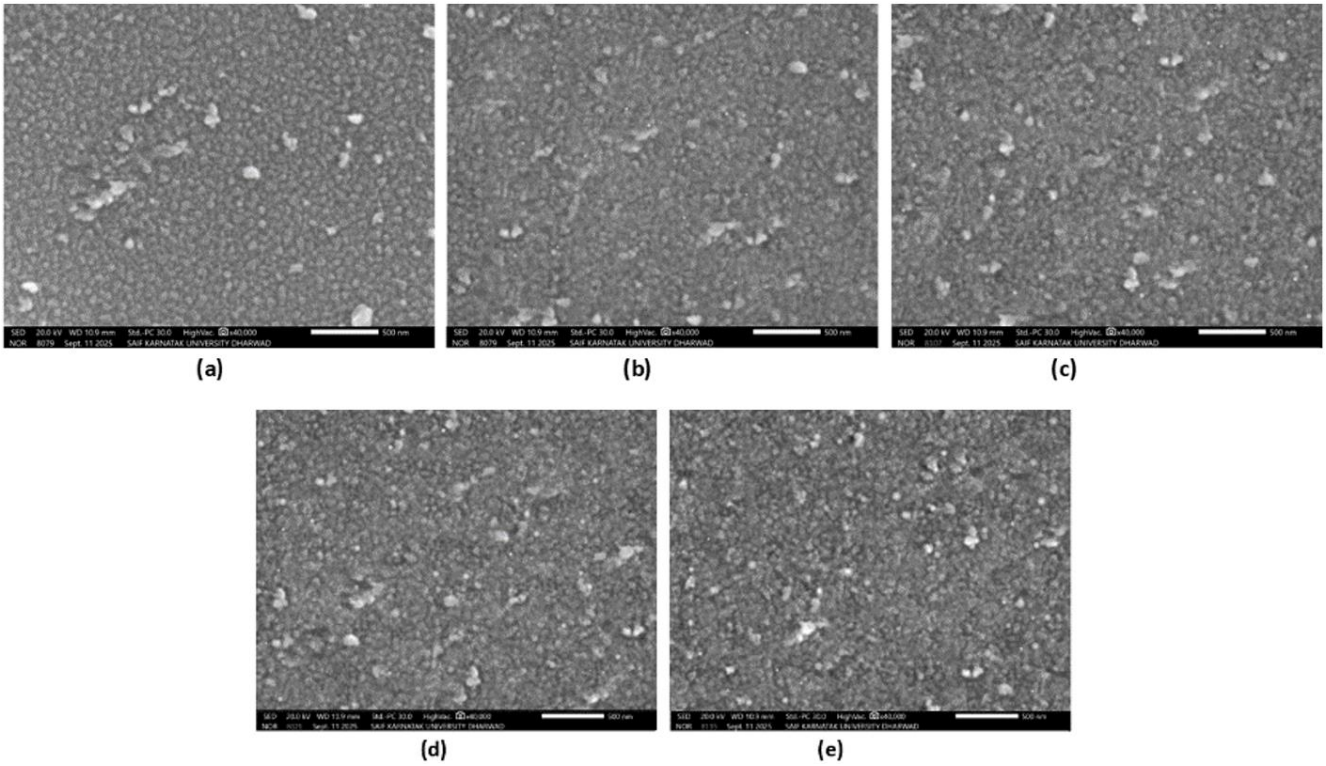

Figure 2. *SEM images of $ZrFe_{2-x}Bi_xO_5$ at (a) x = 0, (b) 0.25, (c) 0.50, (d) 0.75, (e) 1.00.*

SEM images reveal a clear and progressive response of surface morphology to Bi substitution. The undoped parent compound (Figure 2a) shows large, irregularly shaped, angular grain clusters separated by conspicuous inter-grain voids. The comparatively broad particle size distribution and high porosity are consistent with the large crystallite size (32.1 nm) and low dislocation density ($\rho = 3.08 \times 10^{13}$ m^{-2}) documented in Table 1; scattered bright protrusions are attributable to topographic secondary-electron contrast enhancement at surface asperities rather than chemical inhomogeneity [32].

As x increases from 0.25 to 1.00 (Figures 2b-2e), the microstructure evolves markedly toward a finer, more densely packed assembly. For x = 0.25 and 0.50, grains appear polygonal facets, inter-grain contact area grows with multi-domain grains, each encompassing several coherently scattering XRD crystallite domains. For x = 0.75 and 1.00, grain boundaries are sharply defined and porosity diminishes markedly. The grain-size with Bi content mirrors the crystallite refinement in Table 1 and is attributed to the elevated elastic energy around oversized Bi^{3+} centres impeding grain-boundary migration, an effect analogous to Zener pinning [33, 34]. EDAX analysis (Table 2) confirms Zr, Fe, Bi, and O in stoichiometric proportions without extraneous peaks, establishing phase purity consistent with the XRD data.

Table 2. *EDAX elemental atomic percentages for $ZrFe_{2-x}Bi_xO_5$ compositions.*

Composition (x)	Atomic%			
	Zr	Fe	Bi	O
0	10.54 ± 0.6	23.02 ± 1.04	0	66.44 ± 3.05
0.25	10.58 ± 0.7	20.12 ± 0.8	3.04 ± 0.3	66.26 ± 3.08
0.50	10.56 ± 0.5	17.27 ± 0.6	5.77 ± 0.5	66.40 ± 3.02
0.75	10.59 ± 0.8	14.35 ± 0.3	8.86 ± 0.6	66.20 ± 3.11

Composition (x)	Atomic%			
	Zr	Fe	Bi	O
1.00	10.53 ± 0.6	11.53 ± 0.3	11.01 ± 0.7	66.93 ± 3.15

3.3. Magnetic Properties

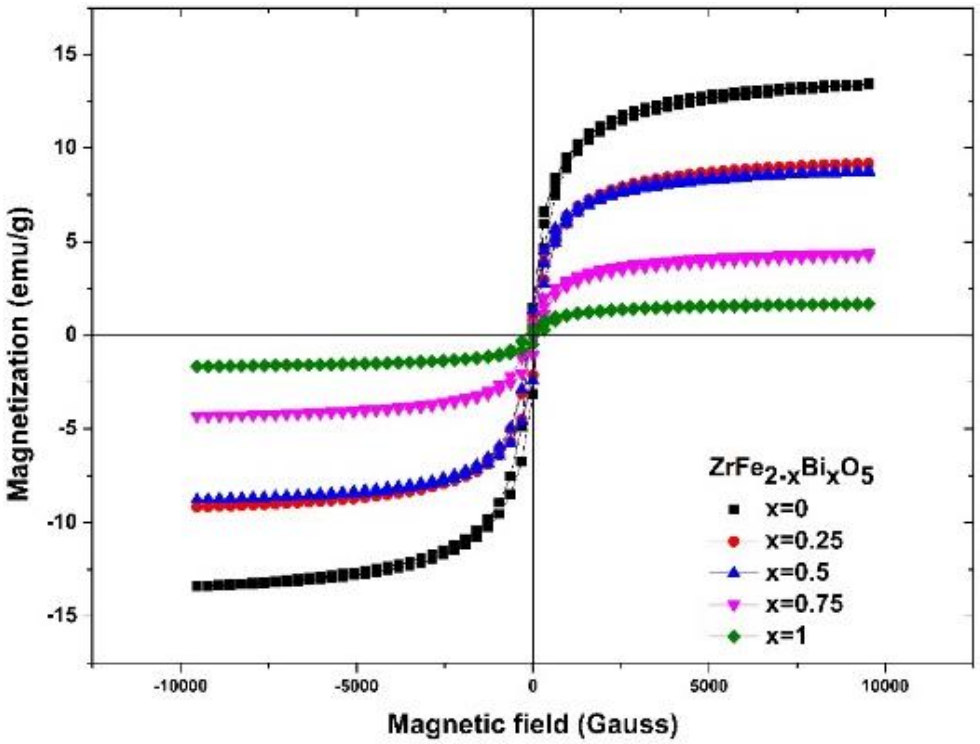

Figure 3. Room-temperature M-H loops of $ZrFe_{2-x}Bi_xO_5$ compositions.

Room-temperature M-H loops recorded over ±10 kOe (Figure 3) are open and relatively narrow for every composition, the characteristic signature of soft ferromagnetic behaviour. The squareness ratio S ranges from 0.165 (x = 0) to 0.252 (x = 1.00), comfortably below the 0.5 threshold that the Stoner-Wohlfarth model [35] identifies with single-domain particles. Such S values indicate a multi-domain ferromagnetic ground state [36, 37] in which reversal is governed by Bloch-wall displacement rather than coherent spin rotation, consistent with the SEM-derived apparent grain diameters of 45-90 nm that comfortably exceed the single-domain radius for iron-oxide-class ceramics [36]. All derived magnetic parameters are collected in Table 3.

M_s falls from 16.46 emu g^{-1} at x = 0 to 1.67 emu g^{-1} at x = 1.00, a 90% suppression. Comparison with our previous investigation [11] is instructive: over x = 0-0.05, Ni^{2+} doping reduced M_s by only ~31%. The disparity directly reflects the magnetic valence contrast between the two dopants Ni^{2+} (d^8, 2 μ_B) partially maintains the sublattice moment, whereas Bi^{3+} ($6s^2$, 0 μ_B) contributes no spin and simultaneously severs Fe-O-Fe superexchange bridges [38, 39]. Magnetic moment per formula unit n_B was calculated using following formula n_B [40, 41].

$$n_B = \frac{Molecular\ \ Weight\ \ XM_S}{5585} \quad (1)$$

n_B drops from 0.834 μ_B to 0.130 μ_B across the series. A marginal non-monotonic bump between x = 0.25 (0.527 μ_B) and x = 0.50 (0.565 μ_B) is a molecular-weight artefact, the formula weight increases by nearly 38 g mol^{-1} in this step while M_s barely changes and carries no independent physical significance [42].

H_c climbs monotonically from 102.24 G (x = 0) to 182.22 G (x = 1.00), a 78% overall gain that contrasts sharply with the near-constant coercive field (~100-103 G) in the Ni-doped system [11]. Three independent mechanisms, each corroborated by XRD or SEM data, drive this coercivity increase. (i) Grain-boundary pinning: the denser grain-boundary network in finer-grained samples (Section 3.2) multiplies Bloch-wall

pinning sites [36, 37]. (ii) Magnetoelastic coupling to lattice microstrain: the doubling of ε (Table 1) creates local anisotropy gradients that resist domain-wall motion [43, 44]. (iii) The stereochemically active Bi^{3+} $6s^2$ lone pair induces off-centre oxygen displacements [19] that lower local symmetry and scatter walls. The disproportionate H_c jump between x = 0.75 (133.1 G) and x = 1.00 (182.22 G) is consistent with the lone-pair effect becoming percolative once Bi^{3+} is the majority B-site occupant.

Table 3. *Room Temperature Magnetic parameters for $ZrFe_{2-x}Bi_xO_5$ compositions.*

Composition (x)	Saturation Magnetization M_s (emu g^{-1})	Remanent Magnetization M_r (emu g^{-1})	Coercive Field H_c (Gauss)	Squareness Ratio $S = \frac{M_r}{M_s}$	Magnetic Moment n_B (μ_B)
0	16.46	2.71	102.24	0.1646	0.834
0.25	9.17	1.88	106.23	0.2050	0.527
0.50	8.78	1.56	125.20	0.1777	0.565
0.75	4.35	0.85	133.10	0.1954	0.310
1.00	1.67	0.42	182.22	0.2515	0.130

3.4. Impedance Properties

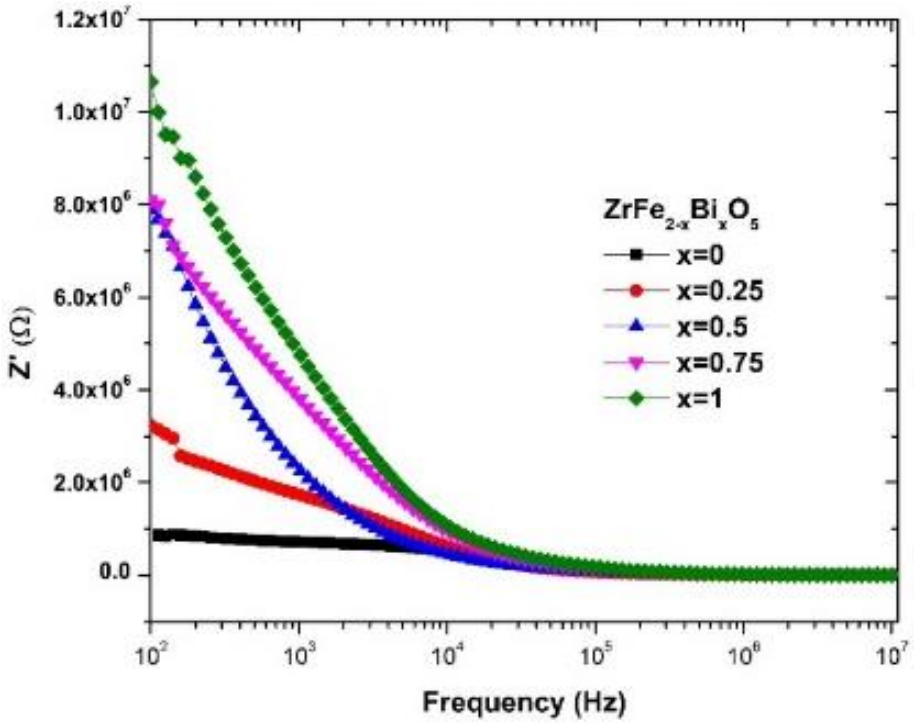

Figure 4. *Real part of impedance Z′ versus frequency for $ZrFe_{2-x}Bi_xO_5$ compositions.*

The real component of impedance Z′ (Figure 4) is high at 100 Hz and decreases steadily with frequency for all compositions, all curves converging near zero above nearly 10^5 Hz. The magnitude at 100 Hz rises from nearly 0.8 MΩ (x = 0) to ~10.5 MΩ (x = 1.00), with intermediate compositions taking values of nearly 3.0, 6.0, and 8.0 MΩ. Within the Maxwell-Wagner-Koops microstructural model [45-47], the high Z′ at low frequency reflects the dominant role of highly resistive grain boundaries, while the convergence to low values at high frequency indicates that charge carriers interact principally with the more conductive grain interiors. Bi^{3+} incorporation reduces the concentration of mobile Fe^{3+}/Fe^{2+} hopping pairs, simultaneously raising grain-bulk and grain-boundary resistance. Nickel doping in our prior study [11] showed the

same qualitative trend but with far smaller magnitudes, consistent with the much lower substitution levels used ($x \leq 0.05$) and Ni^{2+} being only weakly hole-forming at the Fe site.

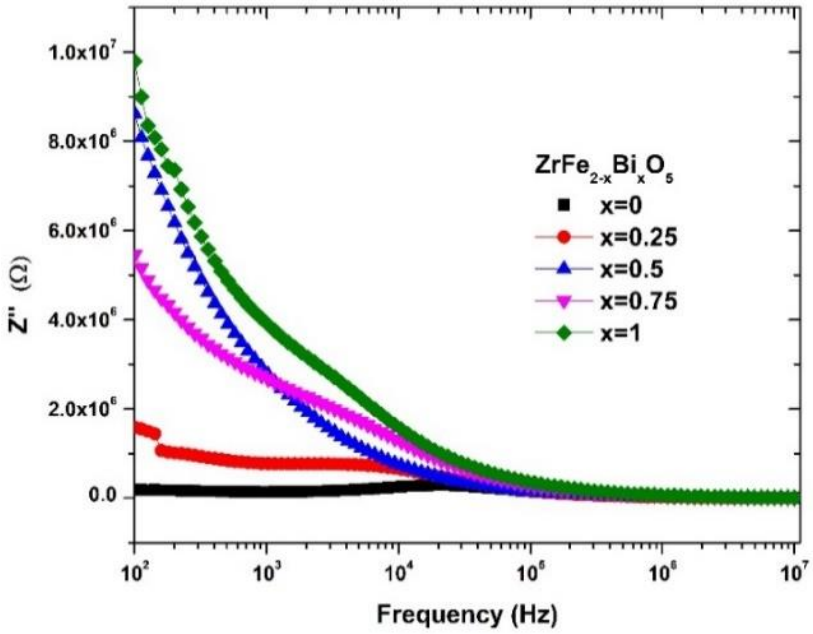

Figure 5. Imaginary part of impedance Z'' versus frequency for $ZrFe_{2-x}Bi_xO_5$ compositions.

The imaginary part Z″ (Figure 5) follows an analogous monotonic decay from large values at 100 Hz toward zero at high frequency, with the amplitude hierarchy x = 1.00 > 0.75 > 0.50 > 0.25 > 0 at any given low frequency. The absence of a resolved Z″ maximum within the measurement window (100 Hz-10 MHz) for $x \geq 0.50$ indicates that the predominant relaxation frequency lies below 100 Hz, i.e., the grain-boundary arc is too large to be fully captured in the accessible frequency range. This is a direct consequence of the large R_{gb} values documented in the equivalent-circuit fitting. The combined Z′ and Z″ behaviour is characteristic of non-Debye type relaxation [48, 49], arising from a distribution of relaxation times across grain-boundary regions of varying thickness, composition, and local Bi^{3+} enrichment.

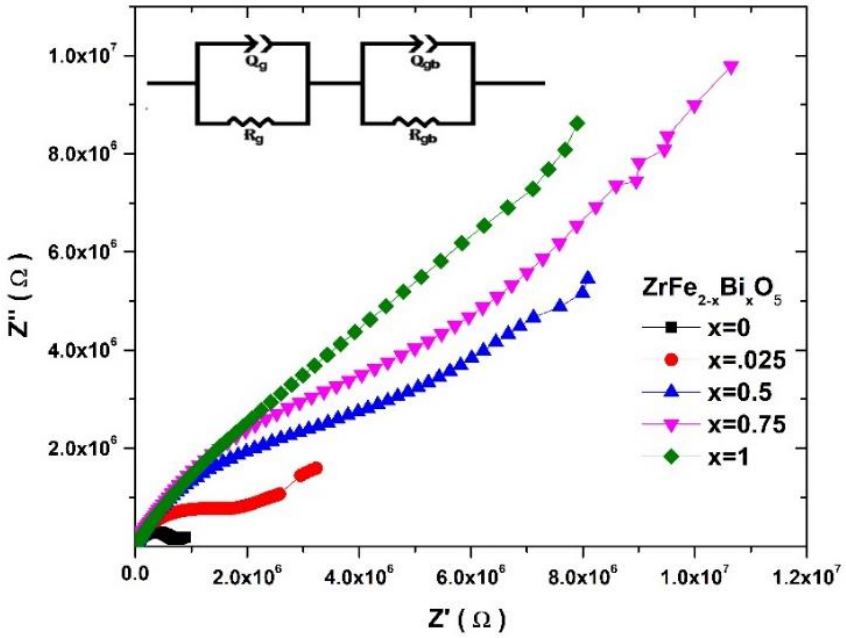

Figure 6. Nyquist plots (Z'' vs Z') for $ZrFe_{2-x}Bi_xO_5$ compositions with equivalent circuit.

Complex impedance Nyquist plots for all compositions are shown in Figure 6. For x = 0, the arc spans an extremely small impedance range compare to doped one and lies almost entirely within the noise floor of the plot, consistent with the high AC conductivity of this composition. For x = 0.25, a partially resolved, depressed semicircular arc is discernible. At x ≥ 0.50, the data trace large-radius arcs whose low-frequency limbs fall outside the measurement window (100 Hz), so only the ascending portions are captured. The depression of all arcs below the real axis confirms non-Debye type relaxation [49, 50], arising from a distribution of relaxation times rather than a single exponential process.

All data were fitted to the equivalent circuit ($R_g||CPE_g$) + ($R_{gb}||CPE_{gb}$), where two parallel constant phase element and resistor units are connected in series, with the grain element ($R_g||CPE_g$) dominating at high frequency and the grain-boundary element ($R_{gb}||CPE_{gb}$) at low frequency [47, 50, 51]. All fitted parameters are tabulated in Table 4.

Table 4. *Equivalent circuit parameters from Nyquist plot fitting for $ZrFe_{2-x}Bi_xO_5$ compositions.*

Composition x	Grain Resistance Rg (Ω)	Grain CPE Qg (F)	Grain CPE Phase Exponent ng	Grain Boundary Resistance Rgb (Ω)	Grain Boundary CPE Qgb (F)	Gran Boundary CPE Phase Exponent ngb	Chi Square Value χ2
0	6.03×10^{5}	3.55×10^{-11}	0.9079	1.28×10^{6}	2.02×10^{-7}	0.3912	6.63×10^{-4}
0.25	1.78×10^{6}	1.43×10^{-10}	0.7907	4.37×10^{6}	2.61×10^{-9}	0.7711	6.32×10^{-3}
0.50	3.24×10^{6}	3.87×10^{-10}	0.7600	6.48×10^{6}	1.93×10^{-10}	0.7923	1.15×10^{-2}
0.75	5.16×10^{6}	6.94×10^{-10}	0.7441	9.37×10^{6}	1.14×10^{-10}	0.8136	1.82×10^{-2}
1.00	7.82×10^{6}	1.12×10^{-9}	0.7218	1.36×10^{7}	6.87×10^{-11}	0.8312	2.55×10^{-2}

Trends in Table 4 are evident that both R_g and R_{gb} increase monotonically from x = 0 through x = 1.00 (R_g: 6.03 × 10^5 to 7.82 × 10^6 Ω; R_{gb}: 1.28 × 10^6 to 1.36 × 10^7 Ω), confirming that Bi^{3+} incorporation progressively impedes charge transport in both microstructural regions. The CPE coefficient Q_g rises steadily from 3.55 × 10^{-11} to 1.12 × 10^{-9} F, consistent with the increase in grain-boundary-to-volume ratio documented by SEM, that is smaller grains = higher specific grain capacitance. Conversely, Q_{gb} decreases by approximately three order of magnitude across the series (2.02 × 10^{-7} to 6.87 × 10^{-11} F), reflecting the progressive reduction in grain-boundary capacitance as the boundary regions become more resistive and the charge accumulation is depleted. The grain phase exponent n_g decreases gradually (0.908→0.722) while n_{gb} increases (0.391→0.831), indicating that grain-interior relaxation becomes more heterogeneous while grain-boundary behaviour approaches that of a more idealised Debye-like capacitor with increasing Bi content, a trend reported for Bi-containing ferrite composites as well [42, 52]. For all compositions $R_{gb} > R_g$ and $Q_{gb} > Q_g$, a well-established hallmark of polycrystalline ionic oxides where grain boundaries offer a higher energy barrier than bulk grains [47, 50, 51].

3.5. Dielectric Properties

The dielectric constant ε′ and dielectric loss ε″ are determined from the measured capacitance C and dissipation factor tan δ [53, 54]:

$$\varepsilon' = \frac{Cd}{\varepsilon_0 A} \tag{2}$$

$$\varepsilon'' = \varepsilon' \tan\delta \tag{3}$$

where d is pellet thickness, A the electrode area, and ε_0 the permittivity of free space. At 100 Hz, ε′ spans nearly two decades across the series: from nearly 5 × 10^4 for $ZrFe_2O_5$ to nearly 10^3 for x = 1.00 (Figure 7). By 10 MHz all curves converge to ε′ values in the range 10-30, where only intrinsic lattice polarization mechanisms contribute. The high low-frequency ε′ and its steep frequency dependence are the textbook signature of Maxwell-Wagner-Sillars (MWS) space-charge polarization [45-47]: at low frequencies, charge carriers accumulate at resistive grain boundaries on a timescale exceeding the field period, generating giant effective permittivities; at high frequencies, carriers cannot follow the rapidly alternating field and ε′ plateaus near its intrinsic value. Bi substitution reduces ε′ because the Verwey-type [55] $Fe^{3+}\leftrightarrow Fe^{2+}$ electron hopping that generates the mobile space charge is progressively diluted as Bi^{3+} occupies Fe sites, in direct analogy to the behaviour documented for Ni^{2+} doping in our prior study [11] and for Bi^{3+}-bearing spinel ferrites in the wider literature [42, 52, 56].

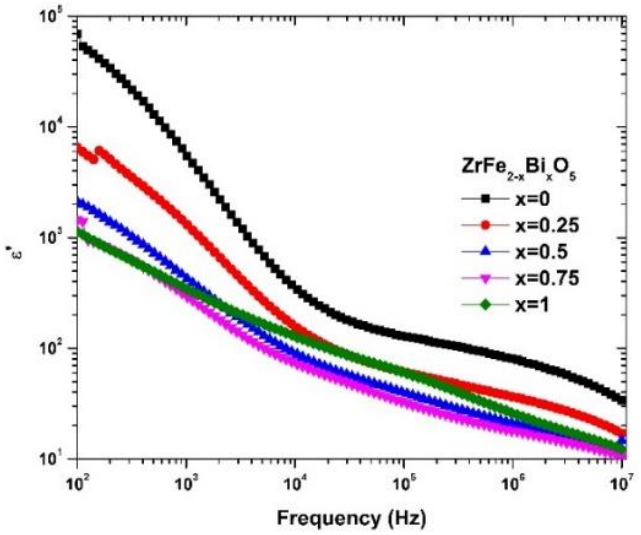

Figure 7. *Dielectric constant ε′ vs frequency of $ZrFe_{2-x}Bi_xO_5$ compositions.*

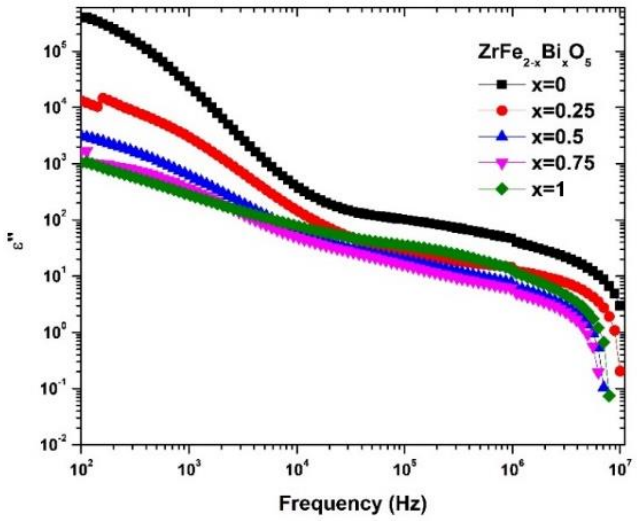

Figure 8. *Loss tangent tanδ vs frequency of $ZrFe_{2-x}Bi_xO_5$ compositions.*

The dielectric loss ε″ (Figure 8) follows the same monotonically decreasing frequency dependence and scales proportionally with ε′ at each composition, as expected when ohmic conduction losses dominate at low frequencies. At high frequencies ε″ drops toward intrinsic polarization loss values and Bi doping reduces ε″ across the full frequency window, confirming suppression of conduction-driven polarization.

The loss tangent tanδ (Figure 9) begins at nearly 8-9 at 100 Hz for $ZrFe_2O_5$ and decreases to nearly 1-1.5 for $x \geq 0.50$. A broad shoulder centred near 10^3-10^4 Hz for the x = 0 and 0.25 compositions signals a dielectric relaxation process; the absence of a sharp, symmetric Debye-type peak is the hallmark of non-Debye relaxation [48, 57], arising from a distribution of relaxation times across grain-boundary regions of heterogeneous thickness and local composition. This shoulder attenuates and shifts with increasing Bi content as Fe hopping pairs become fewer [11, 55, 56]. Above 10^6 Hz, tanδ drops sharply for all compositions, indicating that polarization mechanisms can no longer track the rapidly alternating field. The progressive suppression of tanδ with x suggests enhanced dielectric stability, analogous to the behaviour of Bi-doped nickel-cobalt ferrites [52, 58] and Ni-doped copper ferrite [59].

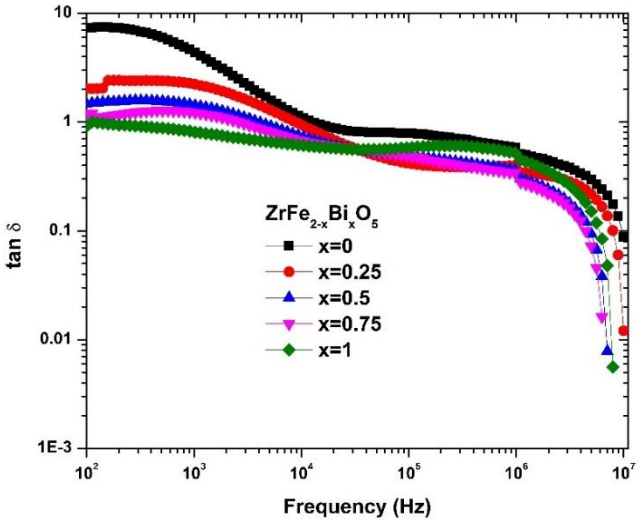

Figure 9. *Dielectric loss ε″ vs frequency of $ZrFe_{2-x}Bi_xO_5$ compositions.*

3.6. AC Conductivity

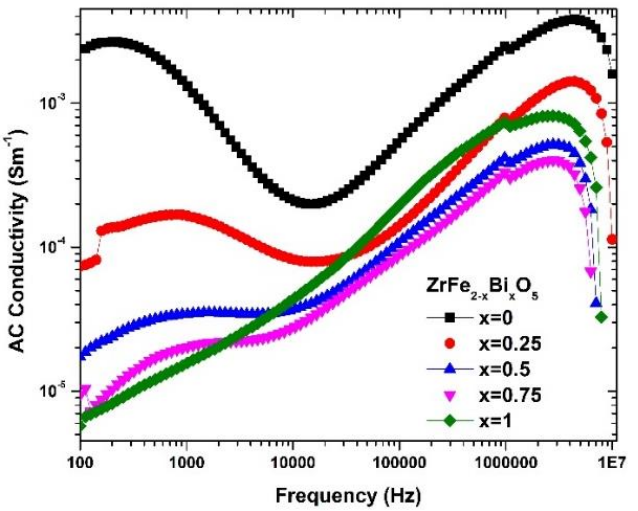

Figure 10. *AC Conductivity vs frequency of $ZrFe_{2-x}Bi_xO_5$ compositions.*

The AC conductivity was calculated from [54, 60]:

$$\sigma_{ac} = 2\pi f \varepsilon_0 \varepsilon' \tan\delta \quad (4)$$

Figure 10 presents the σ_{ac} spectra. The most revealing feature is the characteristic dual-peak structure prominently visible in the x = 0 (black) curve: a low-frequency peak at nearly 100-200 Hz ($\sigma_{ac} \approx 2 \times 10^{-3}$ S m^{-1}), a conductivity minimum near 5×10^3 Hz, and a second peak near 3×10^6 Hz ($\sigma_{ac} \approx 3 \times 10^{-3}$ S m^{-1}). This same fingerprint was documented in the Ni-doped analogue [11] and is interpreted within an established framework. The low-frequency peak arises when the external field frequency matches the characteristic relaxation rate for space-charge accumulation at grain boundaries, including the resonance condition for $Fe^{3+} \rightarrow Fe^{2+}$ carrier hopping across those boundaries; the intermediate conductivity minimum represents the DC-like plateau where neither boundary hopping nor grain-interior processes are resonant; and the high-frequency peak is assigned to short-range, localised Fe^{3+}/Fe^{2+} hopping within grain interiors, generating transient dipoles that relax at the grain characteristic frequency [11, 55, 60].

For x = 0.25, both peaks persist at lower amplitudes (nearly1.5×10^{-4} and nearly 1.5×10^{-3} S m^{-1} for the low- and high-frequency peaks, respectively). From $x \geq 0.50$, the low-frequency peak is no longer resolvable: the grain-boundary hopping carrier density is too dilute to sustain a measurable resonance, and only the high-frequency grain-interior peak remains, its amplitude decreasing from nearly 5×10^{-4} S m^{-1} (x = 0.50) to nearly 3×10^{-4} S m^{-1} (x = 0.75). The slight uptick at x = 1.00 (nearly 8×10^{-4} S m^{-1}) may reflect the onset of percolating Bi-enriched interfacial pathways identified in the SEM micrographs. The universal power-law behaviour $\sigma_{ac} \propto \omega^s$ (Jonscher's law [48]) is broadly obeyed in the intermediate frequency plateau, providing an empirical signature of hopping-type conduction in disordered oxide systems [48, 60].

4. Conclusion

A comprehensive sol-gel auto-combustion study of $ZrFe_{2-x}Bi_xO_5$ (x = 0-1.00) has produced a self-consistent picture linking crystal structure, grain morphology, magnetic response, and broadband electrical behaviour across the full substitution range. Structurally, Bi^{3+} incorporation within the monoclinic C2/c framework obeys Vegard's law (R^2 = 0.9994), expanding the lattice by 1.80% while halving the crystallite size and nearly quadrupling the dislocation density. These XRD-derived changes manifest directly in the SEM microstructures progressive grain refinement, sharpening of grain boundaries, and appearance of Bi-enriched triple-junction inclusions all consistent with size-mismatch driven grain-boundary pinning. Magnetically, the complete spin inactivity of Bi^{3+} drives a 90% collapse of saturation magnetisation while the coercive field rises 78% through three concurrent mechanisms: denser grain-boundary Bloch-wall pinning, magnetoelastic coupling to the doubled lattice microstrain, and local anisotropy from the Bi^{3+} $6s^2$ lone pair. Complex impedance analysis reveals that both grain and grain-boundary resistances increase monotonically from x = 0 to 1.00 (nearly 10 times at 100 Hz), fitted by a two-element CPE equivalent circuit whose parameters evolve in a physically interpretable fashion. Dielectric permittivity decreases with both frequency and Bi content satisfying the Maxwell-Wagner-Sillars framework, and AC conductivity spectra exhibit a dual-peak nature whose progressive attenuation with x quantitatively shows the depletion of Fe^{3+}/Fe^{2+} hopping carriers. All these results demonstrate that Bi^{3+} substitution in $ZrFe_2O_5$ provides a wide and experimentally accessible compositional arrangement for simultaneously tuning soft-magnetic coercivity, dielectric permittivity, and electrical resistance, establishing this system as a promising platform for multifunctional nanoceramics.

Abbreviations

XRD	X-Ray Diffraction
PXRDD	Powder X-Ray Diffraction
SEM	Scanning Electron Microscopy
EDAX	Energy Dispersive X-ray Analysis
VSM	Vibrating Sample Magnetometer
AC	Alternating Current
CPE	Constant Phase Element
MWS	Maxwell–Wagner–Sillars
W-H	Williamson–Hall

Acknowledgments

AM and SM acknowledge the Vision Group on Science and Technology for sanctioning the project under the "Center of Excellence in Science, Engineering and Medicine" (CESEM GRD No 852) Government of Karnataka. SM also, thanks to UGC-DAE Consortium of Scientific Research letter/Order No. 2021-22/03/587 dated 30/03/2022 for the financial support.

Author Contributions

Avadhut Manage: Data curation, Validation, Visualization, Writing – original draft, Writing – review & editing

Balachandra G. Hegde: Conceptualization, Methodology, Project administration, Resources, Supervision, Validation, Writing – review & editing

Shidaling Matteppanavar: Formal Analysis, Investigation, Resources, Validation, Supervision, Writing – review & editing

Conflicts of Interest

Authors don't have any conflict of interest.

References

[1] Thapa, A.; Sharma, B. A review on novel low-dimensional materials based magnetic tunnel junctions: opportunities, challenges, and applications. *Adv. Mater. Technol.* 2025, e00133. https://doi.org/10.1002/admt.202500133

[2] Spaldin, N. A.; Cheong, S. W.; Ramesh, R. Multiferroics: past, present, and future. *Phys. Today* 2010, 63, 38-43. https://doi.org/10.1063/1.3502547

[3] Han Yamin et al. Transition metal oxides: a new frontier in spintronics driven by novel quantum states and efficient charge-spin interconversion. *Front. Mater.* 2024, 11. https://doi.org/10.3389/fmats.2024.1444769

[4] Bhattacharya, A.; May, S. J. Magnetic oxide heterostructures. *Annu. Rev. Mater. Res.* 2014, 44, 65-90. https://doi.org/10.1146/annurev-matsci-070813-113447

[5] Gao, X. M. et al. Characterisation of Fe_2TiO_5 nanocrystallites synthesised via homogeneous precipitation. *Mater. Res. Innov.* 2013, 19, 1-6. https://doi.org/10.1179/1433075X13Y.0000000195

[6] Mahmoud, M. H. H. et al. Physicochemical properties of pseudobrookite Fe_2TiO_5 synthesized from ilmenite ore. *Physicochem. Probl. Miner. Process.* 2019, 55, 290-300. https://doi.org/10.5277/ppmp18131

[7] Lennie, A. R.; Knight, K. S.; Henderson, C. M. B. Cation ordering in $MgTi_2O_5$ (karrooite). *Am. Mineral.* 2007, 92, 1165-1180. https://doi.org/10.2138/am.2007.2322

[8] Dondi, M. et al. Pseudobrookite ceramic pigments: crystal structural, optical and technological properties. *Solid State Sci.* 2007, 9, 362-369. https://doi.org/10.1016/j.solidstatesciences.2007.03.001

[9] Lumpkin, G.; Aughterson, R. Perspectives on pyrochlores, defect fluorites, and related compounds. *Front. Chem.* 2021, 9, 778140. https://doi.org/10.3389/fchem.2021.778140

[10] Newman, R. et al. Synthesis and structure of novel A_2BO_5 compounds. *MRS Adv.* 2018, 3, 1117-1122. https://doi.org/10.1557/adv.2018.210

[11] The authors. Structural, morphological, magnetic, and electrical properties of $ZrFe_{2-x}Ni_xO_5$ nanoparticles (x = 0-0.05) synthesized via sol-gel auto-combustion. *Next Mater.* 2026, 11, 101606. https://doi.org/10.1016/j.nxmate.2026.101606

[12] Shahid, S. et al. Characterization of newly synthesized $ZrFe_2O_5$ nanomaterial and its photocatalytic properties under visible light. *J. Nanomater.* 2013, 2013, 517643. https://doi.org/10.1155/2013/517643

[13] Chakma, S.; Moholkar, V. S. Sonochemical synthesis of mesoporous $ZrFe_2O_5$ and its application for degradation of recalcitrant pollutants. *RSC Adv.* 2015, 5, 53529-53542. https://doi.org/10.1039/C5RA06148B

[14] Mallan, K. P.; Jain, A.; Kalainathan, S. Preparation and magnetic properties of nano size zirconium ferrite particles using coprecipitation method. *Int. J. ChemTech Res.* 2014, 6, 2187-2189.

[15] Abdellahi, M. et al. Introducing $ZrFe_2O_5$ nanopowders for hyperthermia applications. *Chin. J. Phys.* 2018, 56, 880-885. https://doi.org/10.1016/j.cjph.2018.03.024

[16] Khosravi, B. et al. Design and development of a magnetic $ZrFe_2O_4$ nanostructure and its catalytic activities. *J. Iran. Chem. Soc.* 2020, 17. https://doi.org/10.1007/s13738-020-01881-7

[17] Kaur, N. et al. Impact of titanium doping on structural, optical, magnetic and photocatalytic properties of $ZrFe_2O_4$ nanoparticles. *J. Solid State Chem.* 2025, 350, 125471. https://doi.org/10.1016/j.jssc.2025.125471

[18] Shannon, R. D. Revised effective ionic radii and systematic studies of interatomic distances in halides and chalcogenides. *Acta Crystallogr. A* 1976, 32, 751-767. https://doi.org/10.1107/S0567739476001551

[19] Seshadri, R.; Hill, N. A. Visualizing the role of Bi 6s lone pairs in the off-center distortion in ferromagnetic $BiMnO_3$. *Chem. Mater.* 2001, 13, 2892-2899. https://doi.org/10.1021/cm010090m

[20] Roostaei, S. et al. Sol-gel auto-combustion synthesis of a novel ternary magnetic-recyclable $ZnFe_2O_4/ZnO/CeO_2$ nano-photocatalyst. *Appl. Water Sci.* 2025. https://doi.org/10.1007/s13201-025-02549-4

[21] Niu, B. et al. Sol-gel autocombustion synthesis of nanocrystalline high-entropy alloys. *Sci. Rep.* 2017, 7, 3421. https://doi.org/10.1038/s41598-017-03644-6

[22] Pratheek et al. Design and development of a first order reversal curve measurement enabled variable temperature vibrating sample magnetometer. *Phys. Scr.* 2024, 99, 085932. https://doi.org/10.1088/1402-4896/ad5ca4

[23] Rodríguez-Carvajal, J. Recent advances in magnetic structure determination by neutron powder diffraction. *Phys. B Condens. Matter* 1993, 192, 55-69. https://doi.org/10.1016/0921-4526(93)90108-I

[24] Momma, K.; Izumi, F. VESTA 3 for three-dimensional visualization of crystal, volumetric and morphology data. *J. Appl. Crystallogr.* 2011, 44, 1272-1276. https://doi.org/10.1107/S0021889811038970

[25] Vegard, L. The constitution of mixed crystals and the space filling of atoms. *Z. Physik* 5, 17–26 (1921). https://doi.org/10.1007/BF01349680

[26] Denton, A. R.; Ashcroft, N. W. Vegard's law. *Phys. Rev. A* 1991, 43, 3161-3164. https://doi.org/10.1103/PhysRevA.43.3161

[27] Bragg, W. H.; Bragg, W. L. The reflection of X-rays by crystals. *Proc. R. Soc. Lond. A* 1913, 88, 428-438. https://doi.org/10.1098/rspa.1913.0040

[28] Patterson, A. L. The Scherrer formula for X-ray particle size determination. *Phys. Rev.* 1939, 56, 978-982. https://doi.org/10.1103/PhysRev.56.978

[29] Cullity, B. D.; Stock, S. R. *Elements of X-ray Diffraction*, 3rd ed.; Pearson: Upper Saddle River, NJ, 2001.

[30] Williamson, G. K.; Hall, W. H. X-ray line broadening from filed aluminium and wolfram. *Acta Metall.* 1953, 1, 22-31. https://doi.org/10.1016/0001-6160(53)90006-6

[31] Williamson, G. K.; Smallman, R. E. Dislocation densities in some annealed and cold-worked metals from X-ray Debye-Scherrer measurements. *Philos. Mag.* 1956, 1, 34-46. https://doi.org/10.1080/14786435608238074

[32] Goldstein, J. I. et al. *Scanning Electron Microscopy and X-ray Microanalysis*, 4th ed.; Springer: New York, 2018. https://doi.org/10.1007/978-1-4939-6676-9

[33] Novikov, V. (2000). On Zener pinning in 3-D polycrystals. Scripta Materialia - SCRIPTA MATER. 42. 439-443. https://doi.org/10.1016/S1359-6462(99)00379-6

[34] Yujie Yang et al. The effect of Bi substitution on the microstructure and magnetic properties of the $Sr_{0.4}Ba_{0.3}La_{0.3}Fe_{12-x}Bi_xO_{19}$ hexagonal ferrites *J. Magn. Magn. Mater.* 2017, 422, 209-215. https://doi.org/10.1016/j.jmmm.2004.03.022

[35] Stoner, E. C.; Wohlfarth, E. P. A mechanism of magnetic hysteresis in heterogeneous alloys. *Philos. Trans. R. Soc. Lond. A* 1948, 240, 599-642. https://doi.org/10.1098/rsta.1948.0007

[36] Coey, J. M. D. *Magnetism and Magnetic Materials*; Cambridge University Press: Cambridge, UK, 2010.

[37] Cullity, B. D.; Graham, C. D. *Introduction to Magnetic Materials*, 2nd ed.; Wiley-IEEE Press: Hoboken, NJ, 2009. https://doi.org/10.1002/9780470386323

[38] Ahmad, I. et al. Effects of Ni doping on the structural properties and collapse of magnetic ordering in $NdFe_{1-x}Ni_xO_3$. *Chin. Phys. B* 2016, 25, 028101. https://doi.org/10.1088/1674-1056/25/2/028101

[39] Joshi, S.; Kumar, M. Effect of Ni^{2+} substitution on structural, magnetic, dielectric and optical properties of mixed spinel $CoFe_2O_4$. *Ceram. Int.* 2016, 42, 18154-18165. https://doi.org/10.1016/j.ceramint.2016.08.130

[40] Warsi, M. F. et al. New $LiNi_{0.5}Pr_xFe_{2-x}O_4$ nanocrystallites. *Ceram. Int.* 2017, 43, 14807-14812. https://doi.org/10.1016/j.ceramint.2017.07.228

[41] Gilani, Z. A. et al. New $LiCo_{0.5}Pr_xFe_{2-x}O_4$ nanoferrites for high density storage application. *Ceram. Int.* 2018, 44, 1881-1885. https://doi.org/10.1016/j.ceramint.2017.10.126

[42] Sheikh, F. A. et al. Effects of bismuth on structural and dielectric properties of cobalt-cadmium spinel ferrites. *Chin. Phys. B* 2019, 28, 088701. https://doi.org/10.1088/1674-1056/28/8/088701

[43] Desai, S. S. et al. Influence of Zn-Zr substitution on crystal chemistry and magnetic properties of $CoFe_2O_4$. *Phys. B Condens. Matter* 2020, 596, 412400. https://doi.org/10.1016/j.physb.2020.412400

[44] Amalthi, P.; Vijaya, J. J. Influence of Ni^{2+} doping in structural, magnetic and optical properties of $MnFe_2O_4$. *Mater. Today: Proc.* 2021. https://doi.org/10.1016/j.matpr.2021.04.598

[45] Koops, C. G. On the dispersion of resistivity and dielectric constant of some semiconductors at audio frequencies. *Phys. Rev.* 1951, 83, 121-124. https://doi.org/10.1103/PhysRev.83.121

[46] Wagner, KW (1913), On the theory of imperfect dielectrics. Ann. Phys., 345: 817-855. https://doi.org/10.1002/andp.19133450502

[47] Vaithyanathan, V. et al. Evolution of grain boundary conduction with increasing temperature in pure and Ti-doped Co ferrite materials. *J. Appl. Phys.* 2015, 118, 114102. https://doi.org/10.1063/1.4930589

[48] Jonscher, A. K. The 'universal' dielectric response. *Nature* 1977, 267, 673-679. https://doi.org/10.1038/267673a0

[49] Sinclair, D. C.; West, A. R. Impedance and modulus spectroscopy of semiconducting $BaTiO_3$ showing positive temperature coefficient of resistance. *J. Appl. Phys.* 1989, 66, 3850-3856. https://doi.org/10.1063/1.344049

[50] Srinivas, K.; Sarah, P.; Suryanarayana, S. V. Impedance spectroscopy study of polycrystalline $Bi_6Fe_2Ti_3O_{18}$. *Bull. Mater. Sci.* 2003, 26, 247-253. https://doi.org/10.1007/BF02707799

[51] Adamczyk-Habrajska, M. et al. Impedance spectroscopy of Fe and La-doped $BaTiO_3$ ceramics. *Crystals* 2024, 14, 131. https://doi.org/10.3390/cryst14020131

[52] Sheikh, F. A. et al. Dielectrically modified Dy^{3+} substituted nickel-cobalt ferrites for high frequency devices. *Phys. B Condens. Matter* 2023, 652, 414656. https://doi.org/10.1016/j.physb.2023.414656

[53] Naik, J. et al. Synthesis and characterization of multifunctional $ZnBr_2$/PVA polymer dielectrics. *J. Adv. Dielectr.* 2016, 06, 1650028. https://doi.org/10.1142/S2010135X16500284

[54] Batoo, K. M. et al. Study of dielectric and AC impedance properties of Ti-doped Mn ferrites. *Curr. Appl. Phys.* 2009, 9, 1072-1078. https://doi.org/10.1016/j.cap.2009.03.012

[55] Verwey, E. J.; Haayman, P. W.; Romeijn, F. C. Physical properties and cation arrangement of oxides with spinel structures II: Electronic conductivity. *J. Chem. Phys.* 1947, 15, 181-187. https://doi.org/10.1063/1.1746466

[56] Nyathani, M. et al. Crystal chemistry, magnetic and dielectric properties of nickel-doped strontium ferrites. *Biointerface Res. Appl. Chem.* 2022, 12, 929-939. https://doi.org/10.33263/BRIAC121.929939

[57] Halder, S. et al. Structural, dielectric and electrical characteristics of lead-free electro-ceramic $Bi(Ni_{2/3}Ta_{1/3})O_3$. *Eng. Sci. Technol. Int. J.* 2018, 22. https://doi.org/10.1016/j.jestch.2018.11.007

[58] Malik, R. A. et al. Grain size effects on dielectric, ferroelectric, and piezoelectric properties of modified bismuth sodium titanate ceramics. *J. Eur. Ceram. Soc.* 2019, 39, 1693-1701. https://doi.org/10.1016/j.jeurceramsoc.2018.12.004

[59] Priyadharsini, R. et al. Impact of nickel substitution on structural, dielectric, magnetic, and electrochemical properties of copper ferrite nanostructures. *J. Colloid Interface Sci.* 2024, 653, 917-929. https://doi.org/10.1016/j.jcis.2023.09.113

[60] Rehman, F. et al. Grains and grain boundaries contribution to dielectric relaxations and conduction of $Bi_5Ti_3FeO_{15}$ ceramics. *J. Appl. Phys.* 2015, 118, 214101. https://doi.org/10.1063/1.4936782